

# CbLDM: A Diffusion Model for recovering nanostructure from pair distribution function

Jiarui Cao<sup>† a</sup>, Zhiyang Zhang<sup>† b</sup>, Heming Wang<sup>† a</sup>, Jun Xu<sup>a</sup>, Ling Lan<sup>c</sup>, and Ran Gu<sup>\* b</sup>

<sup>a</sup>School of Statistics and Data Science, Nankai University, Tianjin 300071, China

<sup>b</sup>NITFID, School of Statistics and Data Science, Nankai University, Tianjin 300071, China

<sup>c</sup>Department of Applied Physics and Applied Mathematics, Columbia University, New York, NY, 10027, USA

\*Correspondence e-mail: rgu@nankai.edu.cn

<sup>†</sup>Cao, Zhang and Wang contributed equally to this work.

## Synopsis

The deep learning model CbLDM recovers three-dimensional atomic structures from pair distribution function data. It provides a powerful and efficient tool for determining atomic-scale structural features, accelerating nanomaterial discovery.

## Abstract

Nowadays, the nanostructure inverse problem is an attractive problem that helps researchers to understand the relationship between the properties and the structure of nanomaterials. This article focuses on the problem of using PDF to recover the nanostructure, which this article views as a conditional generation problem. This article propose a deep learning model CbLDM, Condition-based Latent Diffusion Model. Based on the original latent diffusion model, the sampling steps of the diffusion model are reduced and the sample generation efficiency is improved by using the conditional prior to estimate conditional posterior distribution, which is the approximated distribution of  $p(z|x)$ . In addition, this article uses the Laplacian matrix instead of the distance matrix to recover the nanostructure, which can reduce the reconstruction error. Finally, this article compares CbLDM with existing models which were used to solve the nanostructure inverse problem, and find that CbLDM demonstrates significantly higher prediction accuracy than these models, which reflects the ability of CbLDM to solve the nanostructure inverse problem and the potential to cope with other continuous conditional generation tasks.

**Keywords:** Latent Diffusion Model; Condition-based Latent Diffusion Model; Generative Model; Nanostructure inverse problem; Laplacian Matrix

# 1 Introduction

In recent years, nanomaterials have become an important research direction in materials science (Gupta *et al.*, 2019). Due to the size of nanomaterials being close to the electronic coherence length (Billinge, 2019), they exhibit surface effects (Wu *et al.*, 2013), small size effects and macroscopic quantum tunneling effects (Awschalom *et al.*, 1992). These features give nanomaterials extensive application prospects in fields such as electronics, optics, and magnetism (Montero *et al.*, 2002; Cho *et al.*, 2010; Yang & Forrest, 2008; An & Hyeon, 2009). In materials science, nanomaterials display a variety of properties, with one key reason being their structural diversity (Xia *et al.*, 2003; Hu & Wang, 2013). To understand the relationship between structure and property, we focus on the process of inferring the structural characteristics of a nanostructure from its known properties or behaviors, known as the nanostructure inverse problem (Billinge & Levin, 2007; Billinge, 2010).

For solving the nanostructure inverse problem, our focus is on utilizing the pair distribution function (PDF). The advantage of the PDF method over traditional X-ray diffraction (XRD) lies in its ability to integrate all scattering information into the Fourier transform, providing information about atomic distances in nanostructures. This allows the PDF method to better capture features of amorphous or locally ordered structures, making it particularly suitable for complex nanostructures (Fernandez-martinez *et al.*, 2008).

Compared to nuclear magnetic resonance and cryo-electron microscopy, the experimental operation of the PDF method is relatively simple and often does not require complex sample preparation processes (Forse *et al.*, 2015; Hoque *et al.*, 2019). Besides, the data analysis of the PDF method is relatively straightforward, and atomic distance information can be obtained through Fourier transformation, making it easier to interpret and understand.

Traditional methods for the nanostructure inverse problem from PDF data include ab initio methods such as the LIGA algorithm (Juhás *et al.*, 2006; Juhás *et al.*, 2008) and the TRIBOND algorithm (Duxbury *et al.*, 2016), and the Reverse Monte Carlo method (McGreevy, 2001; Soper, 2000). However, these methods have certain limitations. For example, the TRIBOND algorithm is only suitable for small structures with a small number of atoms, and the time complexity is too high for complex structures, while the LIGA algorithm is almost only suitable for highly symmetric structures (Duxbury *et al.*, 2016). The reverse Monte Carlo method is efficient only in highly disordered systems, and is inefficient in solving problems with nearly unique solutions (Billinge, 2008*b*). For the reconstruction of nanostructures with over 100 atoms, traditional methods are time-consuming and imprecise. To address these limitations, finding a more efficient and general solution is crucial.

With the increasing application of artificial intelligence, deep learning methods have been applied to solve this problem. The DeepStruc model (Kjær *et al.*, 2023), based on the Conditional Variational Autoencoder (CVAE), can reconstruct nanostructures from PDFs. CVAE, a generative model,

is an extension of Autoencoder (AE) and Variational Autoencoder (VAE). AE transforms high-dimensional data into low-dimensional vectors through an encoder neural network, and the resulting latent space can be used to reconstruct input data (LeCun, 1987); VAE introduces a regularization term using variational inference, assuming that the low-dimensional representations in the latent space follow a standard normal distribution (Kingma, 2013); CVAE replaces the prior assumption of a standard normal distribution with other conditions (Sohn *et al.*, 2015). Additionally, a classification model called MlstructureMining has been proposed, which obtains potential nanostructure lists by comparing experimental PDFs with simulated PDFs from a database (Kjær *et al.*, 2024). This model is based on the XGBoost ensemble learning algorithm. Although it outperforms deep learning models in classification tasks (Wu *et al.*, 2021), it encounters challenges in generation tasks where deep learning models are more effective. Recently, PXRNet (Guo *et al.*, 2025) shows that diffusion model is effective in solving the nanostructure inverse problem. It uses the diffusion model to recover nanostructure with up to 20 atoms in the cell, but the method is mainly for periodic crystal structure. In contrast, PXRNet uses Powder X-Ray Diffraction(PXRD) to recover nanostructure, and we use PDF data to recover nanostructures. Moreover, our study extends the applicability of the diffusion model to amorphous material and nanostructure with larger numbers of atoms (up to 256).

In this study, our focus lies in utilizing generative neural network to solve the problem. While CVAE stands as a promising concept, incorporating conditional information in the form of PDF to generate corresponding atomic structures (Kjær *et al.*, 2023), models based on VAE exhibit a degree of generative blurriness (Bousquet *et al.*, 2017), leading to less precise predictions. We consider an alternative generative neural network model framework, the Latent Diffusion Model (LDM) (Rombach *et al.*, 2022), which outperforms models under the VAE framework in terms of generative capabilities (Parmar *et al.*, 2021; Rombach *et al.*, 2022). The principle of LDM is to use a pretrained VAE to convert image pixels to a smaller Latent Space, and then perform traditional Diffusion Model inference and optimization in the latent space (Rombach *et al.*, 2022). However, as LDM cannot be directly applied to our specific problem, we leverage the conditional generation nature of our problem, introducing condition information into LDM to accomplish this task, leading to the proposal of the Condition-based Latent Diffusion Model (CbLDM).

In addition to proposing a new model CbLDM, our contributions also include addressing certain details in the process. For instance, an algorithm is developed to accelerate the sampling speed during the model diffusion process, and we replace the atomic distance matrix with the Laplacian matrix for better recovery of the atomic structure. These innovations collectively enhance the accuracy of CbLDM in addressing the nanostructure inverse problem, as demonstrated in our numerical tests.

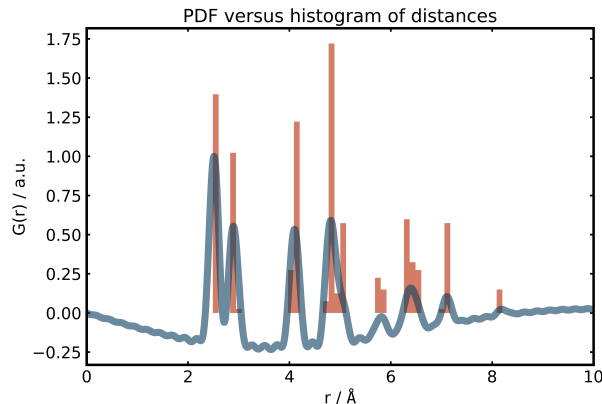


Figure 1: The pair distribution function (PDF)  $G(r)$  versus interatomic distances  $r(\text{\AA})$ , alongside a histogram of atomic distances. The blue curve represents the PDF, while the orange curve shows the histogram of interatomic distances, calculated every 0.2  $\text{\AA}$ . This simulated PDF is derived from a specified structure body centered cubic (BCC).

## 2 Theoretical Foundation

### 2.1 The Pair Distribution Function (PDF)

The pair distribution function (PDF), derived from Fourier transform of normalized and corrected experimental X-ray total scattering data (Proffen *et al.*, 2003; Neder & Korsunskiy, 2005), is a powerful and widely used tool for nanoscale structural analysis (Egami & Billinge, 2012; Billinge & Kanatzidis, 2004). Theoretically, it provides a one-dimensional measure of the probability of finding pairs of atoms separated by a distance  $r(\text{\AA})$  in the powder sample (Billinge, 2008a). Peaks in the PDF correspond to distances with high probability, and as illustrated in Fig. 1, these peaks closely align with a histogram of all interatomic distances in the sample. Consequently, it is possible to extract a list of distances directly from the PDF. This approach has been successfully implemented by fitting the PDF with a model based on the Debye scattering equation (Granlund *et al.*, 2015; Gu *et al.*, 2019).

### 2.2 The Distance Geometry Problem

Using the distance information in the PDF to find the chemical structure can be regarded as an unassigned distance geometry problem (uDGP) (Billinge *et al.*, 2016). To be more specific, it involves finding a set of vertices given the distance list, such that the distances between the vertices correspond one-to-one with the target distance list (Duxbury *et al.*, 2016). Mathematically, uDGP is equivalent to solving a mapping problem between a set (list of interatomic distances) and a graph structure (atomic structure), ultimately mapping the graph structure to three-dimensional coordinates.

If the graph structure of uDGP is given, meaning that the vertex information of each distance is known, it degenerates into the assigned distance geometry problem (aDGP), which is widely used in

protein folding and sensor localization problems (Moré & Wu, 1999; So & Ye, 2007). Although both uDGP and aDGP are NP-hard (Kjær *et al.*, 2023), intuitively uDGP is considered harder because it involves an additional process of assigning edges compared to aDGP, and finding the correct assignment is challenging. Traditional methods like TRIBOND and LIGA incrementally add new atoms on a small structure, incorporating the methods of aDGP in the process of adding new atoms, which involves trial and error leading to frequent backtracking and significant computational costs. The DeepStruc model also considers this uDGP problem, but instead of solving the uDGP directly, it uses a data-driven method to learn the adjacency matrix  $A \in R^{N \times N}$ , where the entries of the adjacency matrix are the Euclidean distance between each pair of the  $N$  atoms. Predicting the adjacency matrix is machine-learning friendly as it can overcome the non-uniqueness of solutions caused by isometric transformations like rotations and translations. The authors then transformed the distance matrix into three-dimensional coordinates by solving the aDGP subproblem.

In this study, our CbLDM approach follows a procedure similar to DeepStruc in that it first transforms the uDGP into an aDGP, after which an aDGP method is applied to recover the three-dimensional coordinates, thereby overcoming the non-uniqueness of solutions caused by isometric transformations such as rotations and translations. Unlike DeepStruc, however, our method replaces the conventional distance matrix in the structural representation graph  $G = (X, A)$  with a Laplacian matrix, which mitigates error propagation from noisy long-range measurements by assigning lower weights to large interatomic distances.

### 2.3 Laplacian Matrix

For an undirected graph  $G(V, E)$  with  $n$  vertices, we consider a fully connected graph here because the PDF covers distance information for all pairs of atoms, although the information for large distances is relatively inaccurate. The Laplacian matrix (Merris, 1994; Lee *et al.*, 2008) is defined by the weighted degree matrix  $D$  and the adjacency matrix  $W$  as  $L = D - W$  with

$$W_{ij} = \exp\left(-\frac{\|v_i - v_j\|_2^2}{2\sigma^2}\right) \text{ and } D_{ii} = \sum_{j=1}^n W_{ij}, \quad (1)$$

where  $v_i$  and  $v_j$  are the vertices of the nanostructure and  $\sigma$  is a parameter. From the definition (1), we know that the larger the distance between  $v_i$  and  $v_j$ , the smaller  $L_{ij}$  is. Therefore, compared to the distance matrix, in Laplacian matrix, small distances are less affected by errors, making it more suitable for PDF data.

In addition, another property of the Laplacian matrix facilitates the subsequent solution of aDGP. For the three-dimensional embedding problem of graph  $G$ , where nearby vertices should remain as close as possible after mapping, this can be formulated as the following optimization problem

$$\min \sum_{i,j} W_{ij} \|z_i - z_j\|_2^2. \quad (2)$$

The solution to problem (2) is equivalent to solving the generalized eigenvalue problem

$$Ly = \lambda Dy,$$

where the eigenvectors corresponding to the three smallest non-zero generalized eigenvalues form the solution. Although this solution is not obtained in terms of mean squared error (MSE), meaning that the Laplacian matrix generated by these three-dimensional coordinates may not be the closest to the target, it still retains certain structural information and serves as a useful initial guess for the aDGP.

## 2.4 Latent Diffusion Model

LDM(Latent Diffusion Model) (Rombach *et al.*, 2022) is a probabilistic generative model, with its diffusion and denoising processes in the latent space. The probabilistic generation model also coincides with the fact that the atomic structure corresponding to the PDF is probabilistic. The latent space can be used to sample the corresponding Laplacian matrix based on the information provided by PDF. We review the principles of LDM in this subsection, which we present in two parts: the VAE and the DDM(Denoising Diffusion Model).

### 2.4.1 Variational Autoencoders

VAE(Variational Autoencoder) is an extension of Autoencoder. It introduces the concept of probability to the traditional Autoencoder, which enables the model to learn the latent distribution of the data and thus has the ability to generate new data (Kingma, 2013; Girin *et al.*, 2020). VAE contains two parts, encoder and decoder. VAE implements the compression process of the data through an Encoder to obtain the posterior distribution  $q_\theta(z|x)$ , and the decompression process of the data through a Decoder to obtain the conditional distribution  $p_\theta(x|z)$ , which represents the probability of generating the observation given the latent variable.  $x$  represents ground truth data,  $z$  represents latent data. VAE assumes the existence of a latent variable  $z$  that controls the data generation process whose joint probability distribution can be decomposed as:

$$p_\theta(x, z) = p_\theta(x|z)p(z)$$

where  $p(z)$  presents prior distribution of  $z$ . Here, we usually assume that  $p(z)$  is  $N(0, I)$ . The loss function of VAE consists of two parts: the reconstruction loss and the KL-divergence, as shown in Eq. (3):

$$\begin{aligned} L(\theta) = & -E_{q_\theta(z|x)}[\log p_\theta(x|z)] \\ & + D_{KL}(q_\theta(z|x)||p(z)) \end{aligned} \quad (3)$$

where  $L$  represents the loss function,  $\theta$  represents the parameters learnt by the model, and  $D_{KL}(q_\theta(z|x)||p(z)) = \int q_\theta(z|x) \log \frac{q_\theta(z|x)}{p(z)} dz$ .

### 2.4.2 Denoising Diffusion Models

DDM(Denoising Diffusion Model) is a generation model based on Markov chain. The working principle of DDM includes two main processes: diffusion process and denoising process. (Ho *et al.*, 2020) Diffusion process gradually adds Gaussian noise to real data  $x_0$  to obtain a final pure Gaussian noise  $x_T$ . In this process, a series of noisy data with different degrees of noise  $x_1, x_2 \cdots x_T$  can be generated. These noisy data and the added Gaussian noise provide a large number of data samples for model training. We assume that the moments are only related to moments throughout the process, and thus the entire diffusion process constitutes a Markov chain. And since its state transfer follows a Gaussian distribution, the Markov chain is called a Gaussian Markov chain. The method of adding noise during diffusion is as Eq. (4).

$$x_t = \sqrt{1 - \beta_t}x_{t-1} + \beta_t\epsilon \quad \epsilon \sim N(0, I) \quad (4)$$

where  $\beta_t$  is a small positive value, representing the value of variance of noise added in time step  $t$ . After a series of derivation, we can get the Eq. (5):

$$\begin{aligned} x_t &= \sqrt{(1 - \beta_1)(1 - \beta_2) \cdots (1 - \beta_t)}x_0 \\ &\quad + \sqrt{1 - (1 - \beta_1)(1 - \beta_2) \cdots (1 - \beta_t)}\epsilon \end{aligned} \quad (5)$$

let  $\alpha = 1 - \beta, \bar{\alpha}_t = (1 - \beta_1)(1 - \beta_2) \cdots (1 - \beta_t)$  and have:

$$x_t = \sqrt{\bar{\alpha}_t}x_0 + \sqrt{1 - \bar{\alpha}_t}\epsilon \quad \epsilon \sim N(0, I) \quad (6)$$

Although theoretically, the process of adding noise from  $x_0$  to  $x_t$  requires  $t$  time steps of noise addition. In fact, it can be obtained in one step from  $x_0$  to  $x_t$  according to the Eq.(6). The denoising process of DDM can be understood as the process of generating  $x_{t-1}$  given  $x_t$ , iteratively generating the final  $x_0$  through Markov chain, and it is also the process that the model needs to learn. The loss function of DDM is represented as Eq.(7).

$$\begin{aligned} L &= E_{q(x_1|x_0)}[-\log_{p_\theta}(x_0|x_1)] \\ &\quad + \sum_{t=2}^T D_{KL}(q(x_{t-1}|x_t, x_0)||p_\theta(x_{t-1}|x_t)) \\ &\quad + D_{KL}(q(x_T|x_0)||p_\theta(x_T)) \end{aligned} \quad (7)$$

where  $p_\theta(\cdot)$  represents the distribution of denoising process that the neural network needs to learn. The third term is a fixed constant that is independent of  $\theta$ , so we don't need to pay attention to it. The first two terms can be further calculated and simplified (Sohl-Dickstein *et al.*, 2015), resulting in a simplified objective function:

$$L_{simple} = E_{t, x_0, \epsilon}[\|\epsilon - \epsilon_\theta(\sqrt{\bar{\alpha}_t}x_0 + \sqrt{1 - \bar{\alpha}_t}\epsilon, t)\|^2]$$

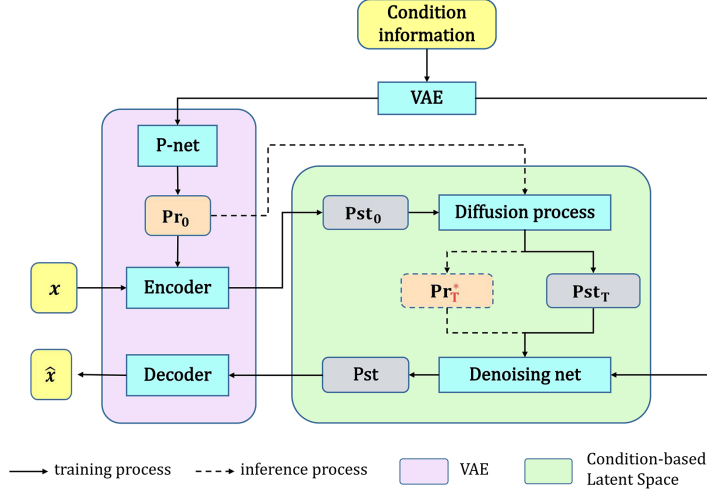


Figure 2: CbLDM Model Architecture

where the  $\epsilon$  represents the real noise added to the data during the diffusion process,  $\epsilon_\theta(\sqrt{\alpha_t}x_0 + \sqrt{1 - \alpha_t}\epsilon, t)$  represents the noise predicted by the reverse denoising network, and  $t$  is sampled from  $\{1, \dots, T\}$ .

In summary, we have introduced VAE and DDM, which together comprise LDM. LDM performs diffusion and denoising on the latent space encoded by VAE, which greatly reduces the computational and memory occupation, and improves the generation efficiency compared to processing directly in the original high-dimensional data space.

### 3 Condition-based Latent Diffusion Model

In this section, we propose a novel framework of Latent Diffusion Model, called Condition-based Latent Diffusion Model (CbLDM), for solving the nanostructure inverse problem with PDF data. During denoising process, by utilizing a conditional prior distribution to estimate  $x_t$  instead of sampling it step by step, we aim to shorten the sampling steps to accelerate the sampling process in conditional generative tasks.

#### 3.1 CbLDM Framework

The entire architecture of CbLDM is shown in Fig. 2. As depicted, CbLDM consists of three main parts: a module to translate and compress conditions into low-dimensional vectors, a Variational Autoencoder to construct a latent space based on conditions and a Diffusion Model to obtain refined latent samples in the latent space.

The first part of CbLDM is a module to translate and compress conditions, aimed at utilizing the conditions more efficiently and effectively. It can take various models as long as it can extract the distinctive characteristics between different conditions. But for continuous conditions, the

encoded vectors should be continuous as well, to maintain the consistency with original conditions. Moreover, if the conditions are already low-dimensional vectors, this module can also act as an identity mapping. The second part is a VAE to construct the latent space. To achieve a latent space with conditional consistency, the prior distribution of the VAE uses a conditional prior distribution instead of normal distribution. By incorporating the conditional prior in the VAE, the latent space can exhibit consistency to some extent both in the original data and the conditions, which can be utilized to train the Diffusion Model and sample new data. The computational demands will be lower than the original Latent Diffusion Model because the Diffusion Model can readily capture the relationship between data and conditions. The third part is the Diffusion Model, which is used for comprehending the relationship between original data and encoded conditions, and getting refined samples of meaningful points in the latent space with conditions from noises.

We employ a VAE model with 1D-convolution layers to compress conditions as the latent embedding. For conditional latent space construction model, we utilize asymmetric convolutional neural networks. In comparison to the Encoder, the Decoder incorporates more Res-Net modules and self-attention layers, while the number of channels in the convolution layer is fewer than that of the Encoder. In the VAE, the prior distribution network consists of MLPs. Compared to LDM (Rombach *et al.*, 2022), our CbLDM introduces conditions during the training of the VAE for compression by replacing the standard normal distribution, typically used as the prior distribution, with a conditional prior distribution. However, unlike CVAE, the decoder of VAE for compression does not incorporate conditional information to assist in the generation, but solely utilizes the sampling points in the latent space for the reconstruction of the original data.

### 3.2 Model Settings

For the three parts of the model mentioned in Section 3.1, we used different training methods, which we will describe in detail in this subsection. As shown in Fig. 2, the training step can be divided into three parts whose training process are described in Alg. 1, Alg. 2 and Alg. 3.

First, we train the model used to comprehend and compress characteristics of conditions. Because the compressed conditions will be used in both next two steps, compressed features can help maintain the conditional consistency in the other VAE and Diffusion Model. In our experiment, the shape of PDF data entered into the conditional vectorization network is (6, 500), and the shape of latent vector is (2,125). As shown in Alg.1,  $c$  represents condition, which is PDF data in our work, and  $z_c$  represents the latent vector of condition. The loss function of the VAE contains two parts: a reconstruction residual ( $L_{rec}$ ) and a KL-divergence between the conditional prior and data posterior, which we assume are both normal distributions (Higgins *et al.*, 2017; Burgess *et al.*, 2018). Here,  $D_c$  and  $E_c$  indicate Decoder and Encoder of VAE,  $q(\cdot)$  represents prior distribution, and  $p_\theta$  represents learnable posterior distribution.

After the compressive VAE for condition converges, we train the other VAE. In our experiment, in order to better obtain the correlation between remote points in Laplacian matrix, we divide

---

**Algorithm 1** Training Compressive VAE for Condition

---

- 1: **repeat**
  - 2:  $c \sim q(c), z_c \sim \mathcal{N}(0, I)$
  - 3: Take gradient descent step on  $\nabla L_{rec}(c, D_c(E_c(c))) + KL(p_\theta(z_c|c)||q(z_c))$
  - 4: **until** converged
- 

the (256, 256) Laplacian matrix into 4 blocks and merge them as (4, 128, 128) tensors due to the existence of multi-attention layer which can capture the relationship effectively. Then, the Encoder constructs a (1, 16, 16) low-dimensional embedding. As shown in Alg.2,  $x$  represents input data, which is Laplacian matrix in our work,  $c_0$  represents compressed feature obtained by the Encoder of compressed VAE for condition,  $z_x$  represents the latent vector of input data, which is related to condition. The loss function is similar to the compressive VAE for condition. In our work, we use Adan (Xie *et al.*, 2024) as the optimizer for training these two VAEs. After the convergence

---

**Algorithm 2** Training Compressive VAE for Input

---

- 1: **repeat**
  - 2:  $x \sim q(x), c \sim q(c), c_0 = E_c(c), z_x \sim q(\mathcal{N}(0, I)|c_0)$ , where  $E_c$  is Encoder of the compressive VAE for condition
  - 3: Take gradient descent step on  $\nabla L_{rec}(x, D_x(E_x(x, c_0))) + KL(p_\theta(z_x|x)||q_\theta(z_x))$ , where  $q_\theta(z_x) = q_\theta(\mathcal{N}(0, I)|c_0)$
  - 4: **until** converged
- 

of both VAEs, we train the Denoising Diffusion Model(DDM) in the latent space constructed by the compressive VAE for input. As normal training process of Denoising Diffusion Probabilistic Model (Ho *et al.*, 2020), we add some Gaussian noise to the latent embedding obtained from the conditional posterior distribution, and use DDM to predict the noise we added. We use U-Net to construct the network for the latent space diffusion model to complete the task of reconstructing the (1, 16, 16) low-dimensional coding from noise. As shown in Alg.3,  $z_0$  indicate the latent embedding obtained from the conditional posterior which is trained at compressive VAE for input. The other parameters are similar to the parameters in DDM and before. The loss function of DDM is  $L_1$  loss between the added noise and predicted noise. For the training for DDM, we use AdamW (Loshchilov, 2017) as the optimizer.

---

**Algorithm 3** Training DDM

---

- 1: **repeat**
  - 2:  $x \sim q(x), c \sim q(c), c_0 = E_c(c), z_0 \sim q_\theta(z|x, c_0)$ , where  $E_c$  is Encoder of the compressive VAE for condition
  - 3:  $t \sim \text{Uniform}(\{1, \dots, T\})$
  - 4:  $\varepsilon \sim \mathcal{N}(0, I)$
  - 5: Take gradient descent step on  $\nabla_\theta \|\varepsilon - \varepsilon_\theta(\sqrt{\alpha_t}z_0 + \sqrt{1 - \alpha_t}\varepsilon, c_0, t)\|_1$
  - 6: **until** converged
-

### 3.3 Sampling Step

In order to generate new data from simple distribution, Diffusion Model approximate reverse diffusion process through simulating the process of solving a stochastic differential equation (Song *et al.*, 2021). With current sampling methods, the sampling process shall simulate the full extent of reverse diffusion process, which may take much time to synthesize new data. To speed up inference, we raise a new sampling algorithm based on condition for CbLDM. As shown in Fig. 2 and Alg. 4, the sampling process is divided into three steps, and the second step is used to skip part of reverse diffusion process with conditional prior.

---

**Algorithm 4** Sampling

---

- 1: Determine the values of  $T_1$  and  $T_2$
  - 2:  $X_0^* \sim q_\theta(\mathcal{N}(0, I) \mid c_0)$ ;  $\varepsilon_1, \varepsilon_2 \sim \mathcal{N}(0, I)$
  - 3:  $X_{T_1}^* = \sqrt{\bar{\alpha}_1}X_0^* + \sqrt{1 - \bar{\alpha}_1}\varepsilon_1$
  - 4: Sampler  $S$ :  $X_{T_2} = S(\varepsilon_2, T_{\max} \rightarrow T_2)$
  - 5:  $u = \frac{\sqrt{1 - \bar{\alpha}_1}}{\sqrt{1 - \bar{\alpha}_2}}$ ,  $a = \sqrt{\bar{\alpha}_1} - \sqrt{\bar{\alpha}_2} \frac{\sqrt{1 - \bar{\alpha}_1}}{\sqrt{1 - \bar{\alpha}_2}}$
  - 6:  $\hat{X}_{T_1} = aX_{T_1}^* + uX_{T_2}$
  - 7: Sampler  $S$ :  $X_0 = S(\hat{X}_{T_1}, T_1 \rightarrow 0)$
  - 8: **return**  $X_0$
- 

The first step is to decide how many timesteps will be skipped during the sampling, and then determine  $T_1$  and  $T_2$  according to different proportion of the noise added to training data in different time. Here  $T_1$  is the time point at which the conditional prior sample is noised, and  $T_2$  is the time point at which the Gaussian noise is denoised. The second step is to obtain a  $T_2$  sample called  $X_{T_2}$  that is denoised from Gaussian noise, and a  $T_1$  sample called  $X_{T_1}^*$  that is noised from conditional prior. We then use  $X_{T_2}$  and  $X_{T_1}^*$  with Eq. (8) to estimate  $X_{T_1}$  which is the truth sample denoised from Gaussian noise, and obtain  $\hat{X}_{T_1}$ . The last step is to sample predicted data from  $\hat{X}_{T_1}$  with any sampler  $S$  of Diffusion Model. With this conditional sampling algorithm, we can skip the sample process from  $T_2$  to  $T_1$ , which accelerates the speed of the entire sampling process.

$$\hat{X}_{T_1} = (\sqrt{\bar{\alpha}_1} - \sqrt{\bar{\alpha}_2} \frac{\sqrt{1 - \bar{\alpha}_1}}{\sqrt{1 - \bar{\alpha}_2}})X_{T_1}^* + \frac{\sqrt{1 - \bar{\alpha}_1}}{\sqrt{1 - \bar{\alpha}_2}}X_{T_2} \quad (8)$$

Here, the characters in Alg. 4 and Eq. (8),  $X_0^*$  represents the sample of conditional prior  $q_\theta(\cdot|c)$ ,  $X_{T_1}^*$  represents that  $X_0^*$  diffuses from time 0 to  $T_1$ ,  $X_{T_2}$  represents that the generated sample is denoised from Gaussian noise until time  $T_2$ ,  $\varepsilon_1$  and  $\varepsilon_2$  represent Gaussian noise, and  $\bar{\alpha}_1$  and  $\bar{\alpha}_2$  represent the proportion of data at diffusion process which is similar to DDM (Ho *et al.*, 2020). When the VAE converges to an ideal state, we suppose that the conditional approximate posterior  $p_\theta(\cdot|c)$  is approximately equal to the corresponding truth posterior  $p(\cdot|c)$ . And with the assumption that

both conditional prior  $q_\theta(\cdot|c)$  and  $p_\theta(\cdot|c)$  follow normal distributions, they differ by one distribution with finite mean and variance. Based on the above description, we can infer that  $q_\theta(\cdot|c)$  and  $p(\cdot|c)$  differ by only one distribution  $U$  with finite mean and variance.

$$U^* = (\sqrt{\alpha_1} - \sqrt{\alpha_2} \frac{\sqrt{1-\alpha_1}}{\sqrt{1-\alpha_2}})U. \quad (9)$$

With Eq. (8), we can estimate  $X_{T_1}$ , and the error  $U^*$  between truth and estimate is given by Eq. (9). We suppose that the well-learned Diffusion Model has the ability to approximate the correct noise distribution, which can cover the  $U^*$  with enough small interval between  $T_2$  to  $T_1$ . For skipping more steps, we need to maximize the interval which is determined by simulated test dataset. Extremely, if the VAE is not perfect enough, setting  $T_1$  equal to  $T_2$  aligns the sampling process of CbLDM with that of a general Latent Diffusion Model. Conversely, with a perfect VAE, setting  $T_1$  to 0 and  $T_2$  to the maximum value of time means that we only use conditional prior to synthesize.

### 3.4 Algorithm for recovering structures

We change the uDGP into aDGP with deep Learning technology we mentioned before. Our model is able to generate the Laplacian matrix of the nanostructures well through taking the PDF data as a condition. It has not successfully recovered the three dimension structure of the nanostructure atoms in terms of XYZ. It has been previously mentioned that recovering the XYZ coordinates of the atoms from the Laplacian matrix poses an aDGP, and then we have to solve this aDGP.

To recover the three dimension structure, the first step is to symmetrize the Laplacian matrix and regard it as a new Laplacian distance matrix. Subsequently, the eigenvectors corresponding to the three smallest non-zero eigenvalues of the Laplacian matrix are computed and combined as a set of 3D coordinates, which are used as initial values for solving the subsequent optimization problem. Finally, the MSE of the true and predicted values of the Laplacian matrix is minimized using the minimize function in the scipy library (Virtanen *et al.*, 2020), employing the trust region constrained optimization method (Conn *et al.*, 2000).

## 4 Numerical Test

### 4.1 Data Set

The data we use to train is all simulated data, which is simulated by the DiffPy-CMI library (Juhás *et al.*, 2015) and ASE library (Larsen *et al.*, 2017; Bahn & Jacobsen, 2002). Similar to the dataset used in the article (Kjær *et al.*, 2023), we use a dataset of seven structure types for single-metal atomic structure types. Seven structural types are FCC, BCC, SC, HCP, Icosahedral, Decahedral and Octahedral. We use Diffpy-CMI and ASE libraries to generate atomic structure data, and then use Diffpy-CMI library to generate PDF data corresponding to the atomic structure. The

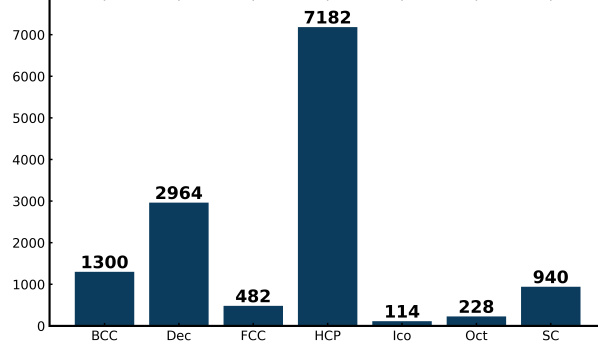


Figure 3: The simulated dataset generated seven structure types of data structures, and the number of different types is shown in the figure.

parameters used to generate experimental PDF data are shown in Tab. 4.1, where Delta2 represents the coefficient for  $(1/r^2)$  contribution to the peak sharpening.

Table 1: Parameters for the generation of simulated PDF data.

Parameter	$r_{\min}$ (Å)	$r_{\max}$ (Å)	$r_{\text{step}}$ (Å)	$Q_{\min}$ (Å <sup>-1</sup> )	$Q_{\max}$ (Å <sup>-1</sup> )	$Q_{\text{damp}}$ (Å <sup>-1</sup> )	$B_{\text{iso}}$ (Å <sup>-2</sup> )	Delta2 (Å <sup>-2</sup> )
Value	0.0	30.0	0.01	0.7	25.0	0 ~ 0.1	0.3	0.0

All structures are generated in the range of 5 to 256 atoms. In total, 13,210 unique structures are generated, and the number of each type in the generated data set is shown in Fig. 3. These data are used as training and validation datasets for CbLDM. We use random seed 42 to use 95% of the data as the training dataset and 5% of the data as the validation dataset. In addition, in order to maximize the interval from  $T_2$  to  $T_1$  that was mentioned in Section 3.3, we generate some additional simulated data which consist of 36 BCC structures and 19 SC structures. In addition to the simulated data used for training or tuning the model as described above, we now introduce the experimental dataset that is only used for testing. The experimental dataset we used is obtained from the study by (Kjær *et al.*, 2023). We have a total of 5 experimental data, which contain PDF without atomic structure information.

In our work, the R-weighted pattern( $R_{wp}$ ) is used to evaluate the generative performance of the model.  $R_{wp}$  is defined by this equation:  $R_{wp} = \left\{ \frac{\sum w_i [Y_i(\text{obs}) - Y_i(\text{calc})]^2}{\sum w_i [Y_i(\text{obs})]^2} \right\}^{\frac{1}{2}}$ , where  $w_i$  represents the weight corresponding to position  $i$ ,  $Y_i(\text{obs})$  represents simulation generated PDF for training,  $Y_i(\text{calc})$  represents model predicted PDF.  $R_{wp}$  reflects the relative residual of the two PDFs and is a reasonable indicator of evaluation.

## 4.2 Results on simulated data

As shown in Fig. 4, we choose data in each of the seven structure types to show the prediction performance of CbLDM on the training dataset. From Fig. 4 we can find that the atomic structure

predicted by CbLDM is very close to the truth atomic structure and the  $R_{wp}$  between their PDFs is small. We also find that CbLDM recovers BCC structure well, but the fluctuation of the residual curves is large. This may be due to the parameters used in fitting the PDF from the structure resulting in a horizontal shift between the predicted PDF and the truth PDF.

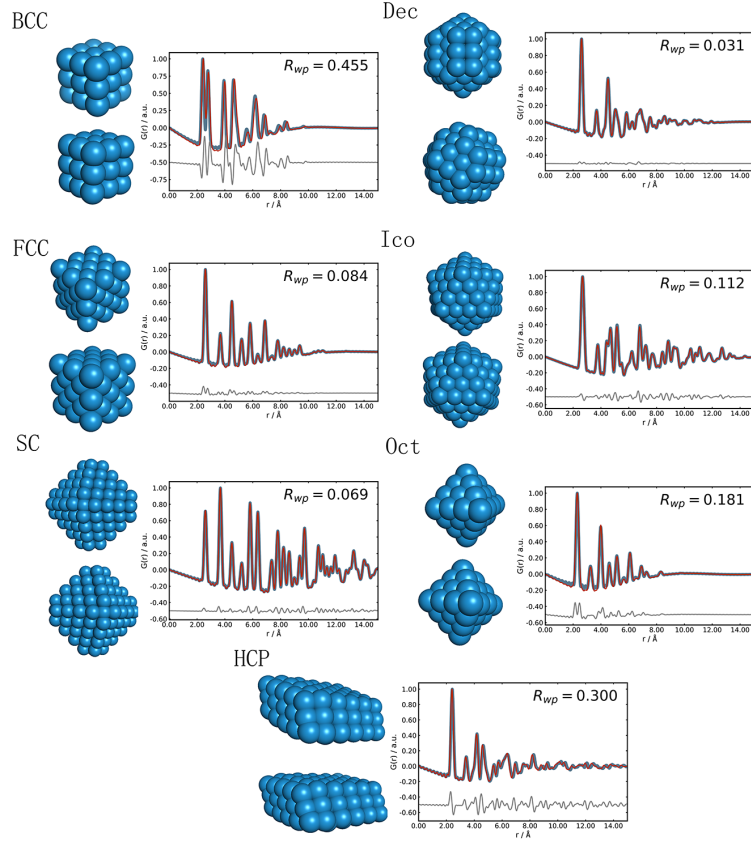


Figure 4: The prediction performance of CbLDM on the training data of seven structure types. Each unit contains three images. The upper left image shows the real structure, the lower left image displays the model-predicted structure, and the image on the right represents a PDF comparison between the two, along with residual curve and  $R_{wp}$  value. The blue curve represents the truth PDF, and the red curve represents the predicted PDF. The residual curve is moved downwards to enhance visibility.

Then, for the seven structure types in Fig.4, we compare the prediction results of models which are MLP, CNN (LeCun *et al.*, 1998), ResNet (He *et al.*, 2016), Transformer (Vaswani, 2017), DeepStruc(CVAE) (Kjær *et al.*, 2023), MLstructureMining(XGBoost) (Kjær *et al.*, 2024) and our Cb-LDM with equal weights  $R_{wp}$ , as shown in Tab. 4.2. For each structure type, we randomly selected 100 structures from the training dataset for the prediction presentation. At the same time, we also randomly selected 1000 structures from the entire training dataset, and the prediction results of different models are shown in the “total” row of Tab. 4.2. The prediction performance of our CbLDM on various structures is better. Through Tab.4.2, we can find that CbLDM has a significant improvement in the prediction of each structure compared to other models. The most obvious one

Table 2:  $R_{wp}$  values of different models on seven different structure types.

	MLP	CNN	ResNet	Trans former	Deep Struc	ML structure Mining	CbLDM
bcc	1.512	1.373	1.358	1.584	0.793	1.196	<b>0.410</b>
dec	1.248	1.197	1.214	1.249	0.692	1.116	<b>0.026</b>
fcc	1.318	1.240	1.286	1.350	1.682	1.221	<b>0.068</b>
hcp	1.234	1.210	1.152	1.244	1.347	1.145	<b>0.263</b>
ico	1.349	1.298	1.273	1.366	1.605	0.459	<b>0.095</b>
oct	1.344	1.277	1.267	1.359	1.590	1.156	<b>0.151</b>
sc	1.431	1.328	1.346	1.478	1.107	0.808	<b>0.059</b>
total	1.278	1.228	1.191	1.299	1.266	1.103	<b>0.380</b>

is the Dec structure, where CbLDM achieves a significantly lower  $R_{wp}$  of 0.026, which indicates superior alignment between predicted and ground-truth PDFs. Meanwhile, CbLDM predicts all seven structures with  $R_{wp}$  within 0.5, which is 50% better than other models on average.

After that, for the validation dataset, we choose some data in each of the seven structure types to visualize the performance of CbLDM. As shown in Fig.5, the first row represents the truth atomic structure and PDF of this data, and the last seven rows represent the atomic structure and PDF predicted by different models. Here we select the Oct structure to compare the performance of different models on the validation data, and the remaining of the structure type comparison graphs are placed in the supplementary. During the model inference process, we find a very interesting

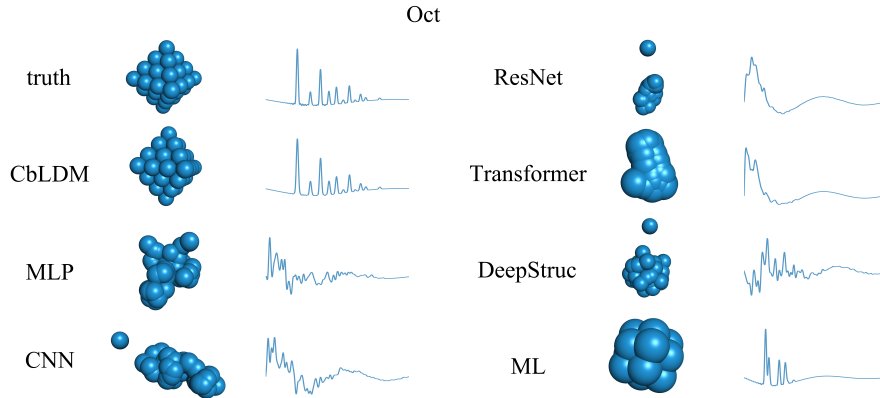


Figure 5: The prediction performance of CbLDM on the validation data of Oct structure. The figure shows, from top to bottom and from left to right, the real data of the Oct structure and the prediction performance of CbLDM, MLP, CNN, ResNet, Transformer, DeepStruc (CVAE), and MLstructureMining (XGBoost). The first and fourth columns in the figure show the model names used, the second and fifth columns show the atomic structures, and the third and sixth columns show their corresponding PDFs.

phenomenon: the model predicts two seemingly different structures, but their PDFs are very similar, as shown in Fig.6. Both structures are Oct structures predicted by CbLDM. The reason for this phenomenon is that the internal stacking of these two structures is the same, but their cross sections are different. This shows that CbLDM fully understands the relationship between PDF and local structures. Through this phenomenon, we find that CbLDM is highly generative and can generate a variety of reasonable structures for users to choose.

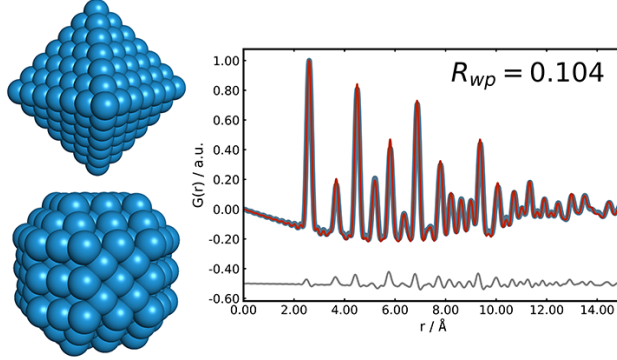


Figure 6: The phenomenon of two seemingly different structures with the similar PDFs. The top left and bottom left are the two atomic structures, and the right is the comparison of PDFs, the residual and  $R_{wp}$ .

### 4.3 Results on experimental data

As shown in Fig.7, we choose to show the prediction performance of CbLDM on two experimental data which are  $Au_{144}(p - MBA)_{60}$  and  $Pt$  nanoparticle. The true structure of  $Au_{144}(p - MBA)_{60}$  is the Dec structure and the true structure of  $Pt$  nanoparticle is the FCC structure. Our CbLDM fits the atomic structure reconstructed from the PDF of both very well. Compared to DeepStruc, CbLDM is able to accomplish structural recovery of the experimental data with fewer generation times, while generating better results. The figure shows the predicted atomic structure of CbLDM on  $Au_{144}(p - MBA)_{60}$  and  $Pt$  nanoparticle and a comparison of the true PDF with the predicted PDF. The test data used on the left side of the figure is  $Au_{144}(p - MBA)_{60}$  and the test data used on the right side is  $Pt$  nanoparticle.

## 5 Conclusion and Discussion

This article focuses on the problem of using PDF data to recover nanostructure. To deal with the conditional generated problem, we propose a new model CbLDM. During the training process, CbLDM replaces the commonly assumed prior distribution in VAE, the standard normal distribution, with a conditional prior distribution, thereby enhancing the continuity of the latent space with respect to conditions. Additionally, CbLDM utilizes the conditional prior distribution to obtain coarse sample points and, through a noise addition process, produces noisy coarse samples. Subse-

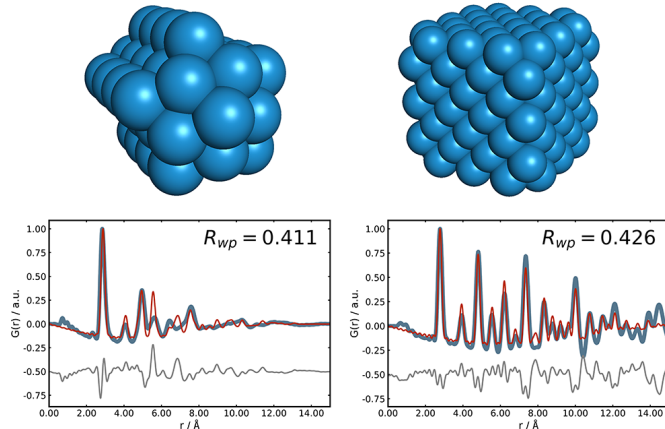


Figure 7: The prediction performance of CbLDM on test data. Two structures are shown here, the predicted atomic structure is shown, and the PDF of the predicted structure is compared with the input PDF

quently, DM is employed to denoise the noisy coarse samples, obtaining refined samples within the latent space based on conditions, which can speed up the denoising process. At the same time, we introduce the Laplacian matrix instead of the traditional distance matrix, which has a smaller error when recovering to the nanostructure. Experimental results demonstrate that CbLDM exhibits significant advantages in conditional generation tasks, particularly showing stronger generalization capabilities and robustness in more complex conditional generation tasks.

In subsequent studies, we will continue to refine the work in this article. For example, the model does not accelerate unconditional generation during sampling and still only samples from random noise. We attempted to incorporate conditional information randomly for generation, but the results were not satisfactory. So we are considering how to embed unconditional information to influence the sampling process. In addition, while CbLDM works very well on simulation generated datasets, there is a lack of data generated from real experiments, which may hinder the model’s ability to generate special structures. We hope to search for more experimental data and the corresponding structures in our future work to expand the dataset and improve the model generalization ability. Finally, we can also conduct ablation experiment to analyze component interactions on CbLDM, which can inform our future work.

## Supplementary Information

Supplementary material related to this article can be found online at TBD.

## Funding

This work was supported by the National Key R&D Program of China grant No.2022YFA1003800, the National Natural Science Foundation of China No.12201318 and the Fundamental Research Funds for the Central Universities No.63253105 for R.G.

**Conflicts of interest:** The authors declare no conflicts of interest.

**Data availability:** The experimental dataset used in this publication is publicly available: <https://huggingface.co/wszzyang/CbLDM>.

The code to train CbLDM and run predictions on the test set is available at <https://github.com/hegwj/CbLDM>.

## References

- An, K. & Hyeon, T. (2009). *Nano Today*, **4**(4), 359–373.
- Anker, A. S., Kjaer, E. T., Dam, E. B., Billinge, S. J., Jensen, K. M. & Selvan, R. (2020). *ChemRxiv*.
- Anker, A. S., Kjær, E. T., Juelsholt, M., Christiansen, T. L., Skjærvø, S. L., Jørgensen, M. R. V., Kantor, I., Sørensen, D. R., Billinge, S. J., Selvan, R. *et al.* (2022). *npj Computational Materials*, **8**(1), 213.
- Awschalom, D. D., DiVincenzo, D. P. & Smyth, J. F. (1992). *Science*, **258**(5081), 414–421. <http://www.jstor.org/stable/2879978>
- Bahn, S. R. & Jacobsen, K. W. (2002). *Computing in Science & Engineering*, **4**(3), 56–66.
- Bao, F., Nie, S., Xue, K., Cao, Y., Li, C., Su, H. & Zhu, J. (2023). In *Proceedings of the IEEE/CVF Conference on Computer Vision and Pattern Recognition*, pp. 22669–22679.
- Belkin, M. & Niyogi, P. (2001). *Advances in neural information processing systems*, **14**.
- Billinge, S. (2008a). In *Powder Diffraction: Theory and Practice*. The Royal Society of Chemistry.
- Billinge, S. J. (2008b). *Journal of Solid State Chemistry*, **181**(7), 1695–1700.
- Billinge, S. J. (2010). *Physics*, **3**, 25.
- Billinge, S. J., Duxbury, P. M., Gonçalves, D. S., Lavor, C. & Mucherino, A. (2016). *4OR*, **14**, 337–376.
- Billinge, S. J. & Kanatzidis, M. G. (2004). *Chemical communications*, (7), 749–760.
- Billinge, S. J. & Levin, I. (2007). *science*, **316**(5824), 561–565.
- Billinge, S. J. L. (2019). *Nanometre-scale structure from powder diffraction: total scattering and atomic pair distribution function analysis*, chap. 5.7, pp. 649–672. John Wiley & Sons, Ltd. <https://onlinelibrary.wiley.com/doi/abs/10.1107/97809553602060000972>
- Blumenthal, L. (1970). *Theory and Applications of Distance Geometry*. AMS Chelsea Publishing Series. Chelsea Publishing Company. <https://books.google.com/books?id=QdcPAQAAMAAJ>
- Bousquet, O., Gelly, S., Tolstikhin, I., Simon-Gabriel, C.-J. & Schoelkopf, B. (2017). *arXiv preprint arXiv:1705.07642*.
- Burgess, C. P., Higgins, I., Pal, A., Matthey, L., Watters, N., Desjardins, G. & Lerchner, A. (2018). *arXiv preprint arXiv:1804.03599*.
- Chen, T. & Guestrin, C. (2016). In *Proceedings of the 22nd acm sigkdd international conference on knowledge discovery and data mining*, pp. 785–794.
- Cho, E. C., Au, L., Zhang, Q. & Xia, Y. (2010). *Small*, **6**(4), 517–522.
- Conn, A. R., Gould, N. I. & Toint, P. L. (2000). *Trust region methods*. SIAM.
- Creswell, A., White, T., Dumoulin, V., Arulkumaran, K., Sengupta, B. & Bharath, A. A. (2018). *IEEE signal processing magazine*, **35**(1), 53–65.
- Dai, B. & Wipf, D. (2019). *arXiv preprint arXiv:1903.05789*.
- Di Wu, Z. W. (2006). *Distance-based protein structure modeling*, p. 10.
- Dong, Q. & Wu, Z. (2002). *Journal of Global Optimization*, **22**, 365–375.
- Duxbury, P. M., Granlund, L., Gujarathi, S., Juhas, P. & Billinge, S. J. (2016). *Discrete Applied Mathematics*, **204**, 117–132.
- Egami, T. & Billinge, S. J. L. (2012). *Underneath the Bragg Peaks: Structural Analysis of Complex Materials*. Newnes.
- Ellersdorfer, P., Petersen, T. C., Opletal, G. & Bedford, N. M. (2021). *Nano Futures*, **5**(2), 022502.
- Eremenko, M., Krayzman, V., Gagin, A. & Levin, I. (2017). *Journal of Applied Crystallography*, **50**(6), 1561–1570.
- Fernandez-martinez, A., Cuello, G. J., Daniels, J. E. & Charlet, L. (2008). *Macra*, **9**, 99–100.

- Forse, A. C., Merlet, C., Allan, P. K., Humphreys, E. K., Griffin, J. M., Aslan, M., Zeiger, M., Presser, V., Gogotsi, Y. & Grey, C. P. (2015). *Chemistry of materials*, **27**(19), 6848–6857.
- Girin, L., Leglaive, S., Bie, X., Diard, J., Hueber, T. & Alameda-Pineda, X. (2020). *arXiv preprint arXiv:2008.12595*.
- Gonçalves, D., Mucherino, A. & Lator, C. (2014). In *2014 Federated Conference on Computer Science and Information Systems*, pp. 457–463. IEEE.
- Granlund, L., Billinge, S. & Duxbury, P. (2015). *Acta Crystallographica Section A: Foundations and Advances*, **71**(4), 392–409.
- Gu, R., Banerjee, S., Du, Q. & Billinge, S. J. (2019). *Acta Crystallographica Section A: Foundations and Advances*, **75**(5), 658–668.
- Guo, G., Saidi, T., Terban, M. W., Billinge, S. J. & Lipson, H. (2024). *ArXiv*, **abs/2406.10796**. <https://api.semanticscholar.org/CorpusID:270560250>
- Guo, G., Saidi, T. L., Terban, M. W., Valsecchi, M., Billinge, S. J. & Lipson, H. (2025). *Nature Materials*, pp. 1–9.
- Gupta, N., Gupta, S. M. & Sharma, S. (2019). *Carbon Letters*, **29**, 419–447.
- He, K., Zhang, X., Ren, S. & Sun, J. (2016). In *Proceedings of the IEEE conference on computer vision and pattern recognition*, pp. 770–778.
- Higgins, I., Matthey, L., Pal, A., Burgess, C. P., Glorot, X., Botvinick, M. M., Mohamed, S. & Lerchner, A. (2017). *ICLR (Poster)*, **3**.
- Ho, J., Jain, A. & Abbeel, P. (2020). *Advances in neural information processing systems*, **33**, 6840–6851.
- Hoque, M. M., Vergara, S., Das, P. P., Ugarte, D., Santiago, U., Kumara, C., Whetten, R. L., Dass, A. & Ponce, A. (2019). *The Journal of Physical Chemistry C*, **123**(32), 19894–19902.
- Hu, S. & Wang, X. (2013). *Chemical Society Reviews*, **42**(12), 5577–5594.
- Ibach, H., Lüth, H., Ibach, H. & Lüth, H. (2009). *Solid-State Physics: An Introduction to Principles of Materials Science*, pp. 21–49.
- Juhás, P., Cherba, D., Duxbury, P., Punch, W. & Billinge, S. (2006). *Nature*, **440**(7084), 655–658.
- Juhás, P., Farrow, C., Yang, X., Knox, K. & Billinge, S. (2015). *Acta Crystallographica Section A: Foundations and Advances*, **71**(6), 562–568.
- Juhás, P., Granlund, L., Duxbury, P., Punch, W. & Billinge, S. (2008). *Acta Crystallographica Section A: Foundations of Crystallography*, **64**(6), 631–640.
- Kingma, D. P. (2013). *arXiv preprint arXiv:1312.6114*.
- Kjær, E., Anker, A. S., Kirsch, A., Lajer, J., Aalling-Frederiksen, O., Billinge, S. J. & Jensen, K. M. Ø. (2024). *Digital Discovery*.
- Kjær, E. T., Anker, A. S., Weng, M. N., Billinge, S. J., Selvan, R. & Jensen, K. M. (2023). *Digital Discovery*, **2**(1), 69–80.
- Lan, L., Liu, C.-H., Du, Q. & Billinge, S. J. (2022). *Journal of Applied Crystallography*, **55**(3), 626–630.
- Larsen, A. H., Mortensen, J. J., Blomqvist, J., Castelli, I. E., Christensen, R., Dulak, M., Friis, J., Groves, M. N., Hammer, B., Hargus, C. *et al.* (2017). *Journal of Physics: Condensed Matter*, **29**(27), 273002.
- Lator, C., Oliveira, A., Rocha, W. & Souza, M. (2021). *Computational and Applied Mathematics*, **40**, 1–10.
- LeCun, Y. (1987). *PhD thesis*.
- LeCun, Y., Bottou, L., Bengio, Y. & Haffner, P. (1998). *Proceedings of the IEEE*, **86**(11), 2278–2324.
- Lee, C.-H., Zaiane, O. R., Park, H.-H., Huang, J. & Greiner, R. (2008). *Information Sciences*, **178**(23), 4501–4511.
- Liu, C., Antypenko, R., Sushko, I. & Zakharchenko, O. (2022). *IEEE Transactions on Reliability*, **71**(2), 1000–1010.
- Loshchilov, I. (2017). *arXiv preprint arXiv:1711.05101*.
- McGreevy, R. L. (2001). *Journal of Physics: Condensed Matter*, **13**(46), R877.
- Menger, K. (1928). *Dimensionstheorie: Karl Menger*. Springer.
- Merris, R. (1994). *Linear algebra and its applications*, **197**, 143–176.
- Montero, M., Liu, K., Stoll, O., Hoffmann, A., Åkerman, J., Martín, J., Vicent, J., Baker, S., Russell, T., Leighton, C. *et al.* (2002). *Journal of Physics D: Applied Physics*, **35**(19), 2398.

- Moré, J. J. & Wu, Z. (1999). *Journal of Global Optimization*, **15**, 219–234.
- Neder, R. B. & Korsunskiy, V. I. (2005). *Journal of Physics: Condensed Matter*, **17**(5), S125.
- Parmar, G., Li, D., Lee, K. & Tu, Z. (2021). In *Proceedings of the IEEE/CVF Conference on Computer Vision and Pattern Recognition*, pp. 823–832.
- Peebles, W. & Xie, S. (2023). In *Proceedings of the IEEE/CVF International Conference on Computer Vision*, pp. 4195–4205.
- Proffen, T., Billinge, S., Egami, T. & Louca, D. (2003). *Zeitschrift für Kristallographie-Crystalline Materials*, **218**(2), 132–143.
- Rombach, R., Blattmann, A., Lorenz, D., Esser, P. & Ommer, B. (2022). In *Proceedings of the IEEE/CVF conference on computer vision and pattern recognition*, pp. 10684–10695.
- Sasaki, H., Willcocks, C. G. & Breckon, T. P. (2021). *arXiv preprint arXiv:2104.05358*.
- Scetbon, M., Elad, M. & Milanfar, P. (2021). *IEEE Transactions on Image Processing*, **30**, 5944–5955.
- So, A. M.-C. & Ye, Y. (2007). *Mathematical Programming*, **109**(2), 367–384.
- Sohl-Dickstein, J., Weiss, E., Maheswaranathan, N. & Ganguli, S. (2015). In *International conference on machine learning*, pp. 2256–2265. pmlr.
- Sohn, K., Lee, H. & Yan, X. (2015). *Advances in neural information processing systems*, **28**.
- Song, Y., Durkan, C., Murray, I. & Ermon, S. (2021). *Advances in neural information processing systems*, **34**, 1415–1428.
- Soper, A. (2000). *Chemical Physics*, **258**(2-3), 121–137.
- Toby, B. & Egami, T. (1992). *Acta Crystallographica Section A: Foundations of Crystallography*, **48**(3), 336–346.
- Vaswani, A. (2017). *Advances in Neural Information Processing Systems*.
- Virtanen, P., Gommers, R., Oliphant, T. E., Haberland, M., Reddy, T., Cournapeau, D., Burovski, E., Peterson, P., Weckesser, W., Bright, J. *et al.* (2020). *Nature methods*, **17**(3), 261–272.
- Wang, K., Gou, C., Duan, Y., Lin, Y., Zheng, X. & Wang, F.-Y. (2017). *IEEE/CAA Journal of Automatica Sinica*, **4**(4), 588–598.
- Wijmans, J. G. & Baker, R. W. (1995). *Journal of membrane science*, **107**(1-2), 1–21.
- Wu, J., Li, Y. & Ma, Y. (2021). In *2021 IEEE 3rd international conference on frontiers technology of information and computer (ICFTIC)*, pp. 457–461. IEEE.
- Wu, Z., Zhang, Y., Jhon, M., Greer, J. & Srolovitz, D. (2013). *Acta Materialia*, **61**(6), 1831–1842.
- Xia, Y., Yang, P., Sun, Y., Wu, Y., Mayers, B., Gates, B., Yin, Y., Kim, F. & Yan, H. (2003). *Advanced materials*, **15**(5), 353–389.
- Xie, X., Zhou, P., Li, H., Lin, Z. & Yan, S. (2024). *IEEE Transactions on Pattern Analysis and Machine Intelligence*.
- Yang, F. & Forrest, S. R. (2008). *ACS nano*, **2**(5), 1022–1032.